

Generation of photonic spin-controlled accelerating light beams along arbitrary curved trajectories

Qingbin Fan^{1,#}, Wenqi Zhu^{2,3,#}, Yuzhang Liang^{1,#}, Pengcheng Huo¹, Cheng Zhang^{2,3}, Amit Agrawal^{2,3},
Xiangang Luo⁴, Yanqing Lu¹, Chengwei Qiu^{5*}, Henri Lezec^{2,*} and Ting Xu^{1,*}

1. *National Laboratory of Solid State Microstructures, College of Engineering and Applied Sciences and Collaborative Innovation Center of Advanced Microstructures, Nanjing University, Nanjing 210093, China.*
2. *Center for Nanoscale Science and Technology, National Institute of Standards and Technology, Gaithersburg, MD 20899, USA.*
3. *Maryland NanoCenter, University of Maryland, College Park, MD 20742, USA.*
4. *Institute of Optics and Electronics, Chinese Academy of Sciences, Chengdu 610209, China.*
5. *Department of Electrical and Computer Engineering, National University of Singapore, 117583, Singapore*

These authors contributed equally.

*Email: xuting@nju.edu.cn, henri.lezec@nist.gov, chengwei.qiu@nus.edu.sg

Bending light along arbitrary curvatures is a captivating and popular notion, triggering unprecedented endeavors in achieving quasi-diffraction-free propagation along a curved path in free-space. Much effort has been devoted to achieving this goal in homogeneous space, which solely relies on the transverse acceleration of beam centroid exerted by a beam generator. Here, based on an all-dielectric metasurface, we experimentally report a synthetic strategy of encoding and multiplexing arbitrary acceleration features on a freely propagating light beam, synergized with photonic spin states of light. Independent switching between two arbitrary visible frequency accelerating light beams with distinct acceleration directions and caustic trajectories is achieved. This proof-of-concept recipe demonstrates the strengths of the designed metasurface element: a subwavelength pixel size, independent control over light beam curvature, multi-wavelength operation in the visible, and ultrathin scalable planar architecture. Our results open up the possibility of creating ultra-compact, high-pixel density and flat-profile nanophotonic platforms for efficient generation and dynamical control of structured light beams.

Bending light beams along engineered curvatures could enable many intriguing phenomena as well as applications that include optical camouflaging [1], cloaking [2], three-dimensional imaging [3], and nanoparticle curved conveyance [4]. However, generating curved light beams usually requires a background media of engineered gradient refractive index [5-6]. The curved trajectory typically expires quickly in a homogeneous medium due to the absence of transverse acceleration of the beam centroid. One solution entails imprinting the incident light beam with a nonlinearly distributed phase profile to realize approximated accelerating light beams (ALBs). As a fascinating caustic-wave phenomenon, ALBs do not diffract while propagating along curved trajectories. For example, optical Airy beams, one representative form of ALB, have shape-preserving nature and their peak intensity follows a continuous parabolic curve as they propagate in free-space [7-8]. Their spatial evolution can be simply described by the paraxial Helmholtz equation, which has a mathematical equivalence with its counterpart Schrödinger equation within the framework of quantum mechanics [9].

Since the first experimental demonstration of optical Airy beams [8], there have been numerous investigations on generalized ALBs that propagate along arbitrary convex trajectories [10], including equivalent demonstrations in other field of physics such as with acoustic beams [11], electron beams [12] or surface plasmon polaritons [13]. Thanks to their unique quasi-non-diffractive nature, ALBs are a subject of intense current interest and have potential for applications in high-resolution microscopy [14], optical manipulation of biological cells [15], generation of light-induced curved plasma channels [16], laser machining of curved microstructures [17] and generation of light bullets [18].

To date, most ALBs are generated by using a commercial spatial light modulator (SLM) [8,10,14-17, 19-21]. However, the large pixel size and pitch of SLMs inherently limits the available range of phase gradient, and its accuracy. As a result, it is difficult to generate ALBs using SLMs with both fine spatial resolution and high precision. Moreover, its bulky footprint and high-cost poses a challenge for their integration within a compact nanophotonic platform. In addition, the

ability to control and multiplex propagation characteristics of an ALB, such as its acceleration direction and caustic trajectory, has long been a challenge. Although some progress has been made towards achieving dynamical control of the propagation trajectory of an ALB using second harmonic generation or three-wave mixing in a nonlinear medium [22-23], these schemes only work at specific frequencies, and impose a stringent requirement on the ALB generation process. Hence, there is a need for realizing efficient generation mechanisms and arbitrary conversion platforms for ALBs that offer subwavelength pixel sizes, compact footprint, low cost and multi-wavelength operation.

In this report, we experimentally realize an ultrathin all-dielectric optical device to circumvent the aforementioned limitations, and provide an efficient platform for both the generation and control of ALBs. In synergy with the photonic spin states of incident light, distinctively generated ALBs can propagate along pre-defined trajectories, independently. Inspired by the classical control methods that utilize phase and polarization of light, we implement an equivalent strategy by using metasurfaces [24-31] – arrays of planar subwavelength optical nanostructures – and controlled by the handedness of the circularly polarized incident light. For experimental proof-of-concept, two all-dielectric metasurface devices operating at visible frequencies are fabricated, exhibiting generation of optical Airy beams with switchable opposite acceleration directions, and dynamic ALBs interchangeable between a natural logarithmic and biquadratic caustic trajectory. The spin state of incident light plays a coordinated role with the encoded polarization-dependent nonlinear phase profile of the dielectric metasurface to generate the requisite ALBs.

Figure 1A depicts an artistic rendering of the metasurface, consisting of an array of subwavelength elliptical dielectric nanoposts. The normally incident light onto the metasurface is assumed to be in two orthogonal spin states: $|R\rangle = \begin{bmatrix} 1 \\ -i \end{bmatrix}$ and $|L\rangle = \begin{bmatrix} 1 \\ i \end{bmatrix}$, where $|R\rangle$ and $|L\rangle$ denote right-circularly polarized (RCP) and left-circularly polarized (LCP) states, respectively. To generate two switchable accelerating beams (ALB₁ and ALB₂), the metasurface is required to provide two independent phase profiles $\varphi_1(x,y)$ and $\varphi_2(x,y)$ corresponding to the incident RCP and LCP spin states, respectively. Hence the metasurface can be described by a Jones matrix

$J(x, y)$ such that it simultaneously satisfies $J(x, y) |R\rangle = e^{i\varphi_1(x, y)} |L\rangle$ and $J(x, y) |L\rangle = e^{i\varphi_2(x, y)} |R\rangle$ [32-33]. Therefore, the Jones matrix $J(x, y)$ takes the form:

$$J(x, y) = \frac{1}{2} \begin{bmatrix} e^{i\varphi_1(x, y)} + e^{i\varphi_2(x, y)} & ie^{i\varphi_2(x, y)} - ie^{i\varphi_1(x, y)} \\ ie^{i\varphi_2(x, y)} - ie^{i\varphi_1(x, y)} & -e^{i\varphi_1(x, y)} - e^{i\varphi_2(x, y)} \end{bmatrix} \quad (1)$$

Based on the eigenvalues and eigenvectors of the Jones matrix in eq. (1), analytical solutions can be obtained for the required orientation angle for each constituent nanopost of the metasurface in the x - y plane, $\theta(x, y)$, relative to the reference coordinate as: $\theta(x, y) = [\varphi_1(x, y) - \varphi_2(x, y)]/4$. The corresponding phase shifts along the elliptical nanoposts' two perpendicular symmetry axes can then be expressed as: $\delta_x(x, y) = [\varphi_1(x, y) + \varphi_2(x, y)]/2$ and $\delta_y(x, y) = \{[\varphi_1(x, y) + \varphi_2(x, y)]/2\} - \pi$, respectively (detailed calculations are shown in the supplementary section SI). Therefore, it is imperative to find a set of nanoposts with proper orientation angle $\theta(x, y)$ and phase shifts $\delta_x(x, y)$ and $\delta_y(x, y)$ covering an entire 2π phase range.

Inset of Fig. 1A shows the artistic rendering of an individual unit-cell of the designed metasurface, composed of elliptical titanium dioxide (TiO_2) nanoposts on a fused-silica substrate. We choose TiO_2 as the constituent material because of its large index of refraction and low loss at visible frequencies [34-36]. The TiO_2 nanoposts are designed to have identical heights of 600 nm but differ in their lateral dimensions D_x and D_y . According to the calculated transmission coefficient and phase shift of cross-polarized scattered light for TiO_2 elliptical nanoposts at a free-space wavelength of 532 nm (supplementary Fig. S1), a set of eight nanostructures, including four fundamental nanoposts with different width (D_x, D_y) and their mirror structures with width (D_y, D_x), is designed which provide eight phase levels covering the 2π phase range for δ_x and δ_y , as shown in Fig. 1B. These structural parameters are optimized such that the nanoposts' polarization conversion efficiencies are relatively high for five different wavelengths across the entire visible range (Fig. 1C), which is a prerequisite for efficient generation of ALBs at multiple wavelengths. All nanoposts are organized in a square array with a lattice constant of $P_x = P_y = 450$ nm along the x and y directions, respectively. This lattice constant is approximately two- to three- orders of

magnitude smaller than the current commercial SLMs for visible light [37]. Thanks to high refractive index of TiO₂, optical fields are mainly confined within individual nanoposts, and hence each one can be regarded as an independent stand-alone cylindrical waveguide (supplementary Fig. S2). Figure 1D-F show the top-view and perspective-view scanning electron microscope (SEM) images of the fabricated TiO₂ metasurface. The complete fabrication process is described in the supplementary section SII.

We first demonstrate a metasurface device capable of generating and switching the acceleration direction of an optical Airy beam. The mapping between the incident and transmitted light through the metasurface follows $|L\rangle \rightarrow |A_l\rangle$ and $|R\rangle \rightarrow |A_r\rangle$, where $|A_l\rangle$ ($|A_r\rangle$) represents the state of Airy beam accelerating towards the left (right). According to the geometrical properties of the optical caustics, ALBs along arbitrary convex trajectories can be generated by direct application of a spatial phase profile on an incident beam [10, 38-39]. Here, we impose a spatial phase function on an incident plane wave to obtain the required phase profile of the metasurface, and generate a two-dimensional Airy beam, expressed as:

$$\varphi_1(x, y) = -\frac{4}{3}\sqrt{n}k(x^{\frac{3}{2}} + y^{\frac{3}{2}}) \quad (2)$$

where n is the acceleration coefficient associated with the contour of the Airy beam (here, $n = 4 \text{ m}^{-1}$), $k = 2\pi/\lambda_0$ is the free-space wavevector and λ_0 is the free-space wavelength of operation. The parabolic caustic trajectory of the Airy beam can be expressed as a form of space curve: $\begin{cases} x = nz^2 \\ y = nz^2 \end{cases}$. The phase profile to generate an Airy beam with opposite acceleration direction can be obtained by $\varphi_2(x, y) = \varphi_1(\sqrt{2}w - x, \sqrt{2}w - y)$, where w is the side length of the square sample ensuring that the output positions of the two Airy beams are centrosymmetric.

The designed metasurface composed of a TiO₂ nanopost array is fabricated with a lateral footprint of $450 \mu\text{m} \times 450 \mu\text{m}$ on a fused-silica substrate. To characterize its performance, a normally incident collimated circularly polarized laser beam at a free-space wavelength of $\lambda_0 = 532 \text{ nm}$ is impinged on the metasurface from the substrate side. A schematic diagram of the measurement setup is shown in supplementary Fig. S3. The parabolic trajectories of the generated accelerating light beam is recorded by mapping the transverse intensity profiles of the transmitted

light beam, with a charge-coupled device (CCD) camera, at different x - y planes on the exit side of the metasurface ($z > 0$, Figure 2A). Under LCP illumination, the metasurface generates an Airy beam with a parabolic trajectory exhibiting a transverse acceleration towards the left side. The main lobe of the Airy beam maintains a spot size of $(30 \pm 1) \mu\text{m}$ up to a propagation distance of ≈ 10 mm, clearly demonstrating the quasi-diffraction-free nature of an ALB propagating along a curved trajectory. The uncertainty in the measurement of the spot size is 1 standard deviation in fitting the full-width half-maximum of the main lobe of the Airy beam. As expected, when the spin state of the incident light is switched from LCP to RCP, a mirrored Airy beam with similar propagation trajectory but opposite acceleration direction is observed. The propagation characteristics and trajectories for both the left- and right- propagating Airy beams match well with the theoretical predictions (shown in Fig. 2B). The experimentally measured Airy beam generation efficiency of the metasurface, defined as the ratio of the optical intensity of the generated ALB to the optical intensity of the incident light beam, is $(52 \pm 2) \%$. The uncertainty in the calculated efficiency is 1 standard deviation based on propagation of uncertainty from the measurements of optical intensities of the transmitted and incident beams using the CCD detectors.

Figure 2C depicts the continuous evolution of the transverse light field at a distance of $z = 8$ mm from the exit surface of the metasurface ($z = 0$ mm) as the spin state of incident light is gradually modified from LCP to RCP using a quarter wave plate (QWP) with a rotation angle α relative to its fast axis increasing from $-\pi/4$ to $+\pi/4$. Since input light with an arbitrary elliptical spin state on the Poincaré sphere is the superposition of two orthogonal spins $|L\rangle$ and $|R\rangle$, the two output states, $|\Psi_l(\alpha)\rangle$ and $|\Psi_r(\alpha)\rangle$, from the metasurface can be respectively expressed as:

$$|\Psi_l(\alpha)\rangle = \cos(\alpha + \frac{\pi}{4}) \cdot e^{-i(\alpha + \frac{\pi}{4})} |L\rangle |A_l\rangle \quad (3)$$

$$|\Psi_r(\alpha)\rangle = \sin(\alpha + \frac{\pi}{4}) \cdot e^{i(\alpha - \frac{\pi}{4})} |R\rangle |A_r\rangle \quad (4)$$

The optical intensity ratio K between these two states can be expressed as $K(\alpha) = \tan^2(\alpha + \frac{\pi}{4})$.

We extract the experimentally measured intensity ratio K for the two opposite Airy beams as a

function of α (supplementary Fig. S4), and find it to be in good agreement with the theoretically predicted values. These results indicate that the intensities of the two generated Airy beams can be tuned by simply changing the spin state of incident light, making it beneficial for the trapping and release of multiple objects during an *in situ* optical manipulation experiment.

In addition to controlling the acceleration direction of ALBs, it is possible to achieve generation and switching between two arbitrary accelerating light beams that follow different caustic trajectories in free-space. As a proof-of-concept, here we report for the first time, a metasurface design that generates two output ALBs, one following a natural logarithmic and another a quartic caustic trajectory, expressed as space curve $C_1: \begin{cases} x = a \ln(bz) \\ y = a \ln(bz) \end{cases}$ and $C_2: \begin{cases} x = cz^4 \\ y = cz^4 \end{cases}$, respectively. The acceleration coefficients a , b and c are freely used as arbitrarily chosen constants, and here $a = -10^{-4}$ m, $b = 8 \times 10^3 \text{ m}^{-1}$, and $c = 6.7 \times 10^4 \text{ m}^{-3}$. The photonic spin-dependent phase profiles of the metasurface corresponding to LCP and RCP incident excitation are respectively expressed as:

$$\varphi_1(x, y) = e^{-1} a^2 b c [2 - \exp(-\frac{x}{a}) - \exp(-\frac{y}{a})] \quad (5)$$

$$\varphi_2(x, y) = -\frac{16}{21} \sqrt[4]{3} c k (x^{\frac{7}{4}} + y^{\frac{7}{4}}) \quad (6)$$

Figure 3 shows the experimental results for this metasurface device illuminated with normally incident circularly polarized light at a free-space wavelength of 532 nm. Figure 3A shows the measured transverse field profiles of two generated ALBs for various x - y planes at different z positions on the exit-side of the metasurface ($z > 0$). Two-dimensional quasi-diffraction-free fields are measured along with their evolution dynamics. When illuminated with a LCP incident light, the accelerating beam generated by the metasurface follows the predesigned natural logarithm trajectory. When the incident light is switched to RCP, the generated beam propagates along a biquadratic curvature. In the latter case, the intensity cross-section of the beam diminishes as the beam propagates farther away from the metasurface exit surface. This occurs because all the side lobes experience rapid deflection, due to the biquadratic transverse acceleration, and begin to converge with the main lobe [10]. Nevertheless, the propagation trajectories of these generated

beams, after passing through an ultrathin dielectric metasurface, validate the theoretical predictions (Fig. 3b). The experimentally measured generation efficiencies for ALBs following natural logarithm and biquadratic caustic trajectories are $(57 \pm 2) \%$ and $(49 \pm 1) \%$, respectively. The uncertainty in the calculated efficiency is 1 standard deviation based on propagation of uncertainty from the measurements of optical intensities of the transmitted and incident beams using the CCD detectors.

Figure 3c shows the continuous evolution of transverse intensity profile at a distance of $z = 5$ mm from the exit surface of the metasurface as the spin state of incident light is gradually changed from LCP to RCP. A gradual monotonic transition between the two distinct accelerating trajectories is clearly evident. Similar to the demonstration with Airy beams discussed above, the intensities of the two arbitrary ALBs can be tuned by changing the spin state along the Poincaré sphere. The theoretical and experimentally measured intensity ratio $K(\alpha)$ for the two ALBs as a function of rotation angle α of the QWP are discussed in supplementary Fig. S4.

Figure 4 shows the experimental results for the two metasurface devices, discussed in the previous sections, illuminated at five different free-space wavelengths across the visible region ($\lambda_0 = 460$ nm, 490 nm, 532 nm, 580 nm, 610 nm). It is clearly evident from the lateral intensity profiles that the transmitted beam still exhibits a two-dimensional Airy-like interference pattern except that the position of main lobe at each wavelength is shifted laterally. The corresponding propagation trajectories for the three types of ALBs are summarized in supplementary Fig. S5-S7. In principle, a two-dimensional ALB can be treated as a superposition of two one-dimensional ALBs travelling along two orthogonal directions. Under the paraxial approximation, for a two-dimensional ALB with a caustic trajectory $C(z)$: $\begin{cases} x = g(z) \\ y = f(z) \end{cases}$, the required phase at the exit surface ($z = 0$) is given by [39]

$$\varphi(x, y) = k[\int g'(z)dx + \int f'(z)dy] \quad (7)$$

where $g(z)$ and $f(z)$ are two continuous functions and respectively indicate the projection of the caustic trajectory of two-dimensional ALB in x - z and y - z plane. As shown in supplementary

Fig. S8, the phase profiles of the TiO_2 metasurface are very similar for the selected multi-wavelengths. Therefore, based on eq. (7), by increasing the free-space wavelength λ_0 hence decreasing k , $\varphi(x, y)$ increases, resulting in a larger deflection for the generated ALB. This prediction agrees well with the experimental observations shown in Fig. 4 and supplementary Fig. S5-S7. The experimentally measured generation efficiencies of the two metasurfaces for ALBs at different wavelengths ranges from $(22 \pm 1) \%$ to $(57 \pm 2) \%$. The uncertainty in the calculated efficiency is 1 standard deviation based on propagation of uncertainty from the measurements of optical intensities of the transmitted and incident beams using the CCD detectors.

Furthermore, as shown in Fig. 4, the acceleration direction and caustic trajectories of the generated ALBs at these multiple incident wavelengths still depend on the spin states of incident light. This occurs because TiO_2 nanoposts have relatively high polarization conversion efficiencies at these wavelengths and can be treated as half-wave plates. As a result, they can generate geometrical phases for the incident light solely based on their rotation angle θ . These wavelength-insensitive geometrical phases are associated with the eigenvectors of the Jones matrix $J(x, y)$ of the metasurfaces, and enable the photonic spin-control functionality [32-33]. Our results explicitly show that these metasurface devices can simultaneously achieve efficient generation and dynamic control of ALBs at multiple wavelengths across the visible region, which are not readily achievable from conventional methods based on SLM.

In conclusion, we have demonstrated an ultrathin all-dielectric metasurface device that can achieve robust generation and arbitrary control of accelerating light beams at multiple wavelength across the visible region. The propagation characteristics of the metasurface-assisted ALBs, including acceleration direction and caustic trajectory, can be well controlled and manipulated. Compared with previous demonstrations of ALB generation, the single layer and ultrathin architecture of the metasurfaces realized here enables an efficient, scalable and integration friendly platform for structured light generation, and its applications.

References

- [1] Han, T. C., Bai X., Thong, J., Li, B. W., & Qiu, C. W. Full Control and Manipulation of Heat Signatures: Cloaking, Camouflage and Thermal Metamaterials. *Adv. Mater.* **26**, 1731–1734 (2014).
- [2] Cai, W., Chettiar, U. K., Kildishev, A. V. & Shalaev, V. M. Optical cloaking with metamaterials. *Nature Photon.* **1**, 224–227 (2007).
- [3] Katz, O., Small, E. & Silberberg, Y. Looking around corners and through thin turbid layers in real time with scattered incoherent light. *Nature Photon.* **6**, 549–553 (2012).
- [4] Soltani, M., Lin, J., Forties, R. A., Inman, J. T., Saraf, S. N., Fulbright, R. M., Lipson, M. Wang, M. D. Nanophotonic trapping for precise manipulation of biomolecular arrays. *Nat. Nanotechnol.* **9**, 448–452 (2014).
- [5] Lynch, D. K. & Livingston, W. C. Color and light in nature. 2nd edn, (Cambridge University Press, 2001).
- [6] Pendry, J. B., Schurig, D. & Smith, D. R. Controlling electromagnetic fields. *Science* **312**, 1780–1782 (2006).
- [7] Siviloglou, G. A. & Christodoulides, D. N. Accelerating finite energy Airy beams. *Opt. Lett.* **32**, 979–981 (2007).
- [8] Siviloglou, G. A., Broky, J., Dogariu, A. & Christodoulides, D. N. Observation of accelerating Airy beams. *Phys. Rev. Lett.* **99**, 213901 (2007).
- [9] Berry, M. V. & Balazs, M. Nonspreading wave packets. *Am. J. Phys.* **47**, 264 (1979).
- [10] Greenfield, E., Segev, M., Walasik, W. & Raz, O. Accelerating light beams along arbitrary convex trajectories. *Phys. Rev. Lett.* **106**, 213902 (2011).
- [11] Zhang, P., Li, T. C., Zhu, J., Zhu, X. F., Yang, S., Wang, Y., Yin, X. B. & Zhang, X. Generation of acoustic self-bending and bottle beams by phase engineering. *Nat. Commun.* **5**, 4316 (2014).
- [12] Voloch-Bloch, N., Lereah, Y., Lilach, Y., Gover, A. & Arie, A. Generation of electron Airy beams. *Nature* **494**, 331–335 (2013).
- [13] Minovich, A., Klein, A. E., Janunts, N., Pertsch, T., Neshev, D. N. & Kivshar, Y. S. Generation and near-field imaging of Airy surface plasmons. *Phys. Rev. Lett.* **107**, 116802 (2011).

- [14] Vettenburg, T., Dalgarno, H. I. C., Nylk, J., Coll-Lladó, C., Ferrier, D. E. K., Čižmár, T., Gunn-Moore, F. J. & Dholakia, K. Light-sheet microscopy using an Airy beam. *Nat. Methods*. **11**, 541–544 (2014).
- [15] Dholakia, K. & Čižmár, T. Shaping the future of manipulation. *Nature Photon.* **5**, 335–342 (2011).
- [16] Polynkin, P., Kolesik, M., Moloney, J. V., Siviloglou, G. A. & Christodoulides, D. N. Curved plasma channel generation using ultraintense Airy beams. *Science* **324**, 229–232 (2009).
- [17] Mathis, A., Courvoisier, F., Froehly, L., Furfaro, L., Jacquot, M., Lacourt, P. A. & Dudley, J. M. Micromachining along a curve: Femtosecond laser micromachining of curved profiles in diamond and silicon using accelerating beams. *Appl. Phys. Lett.* **101**, 071110 (2012).
- [18] Chong, A., Renninger, W. H., Christodoulides, D. N. & Wise, F. W. Airy–Bessel wave packets as versatile linear light bullets. *Nature Photon.* **4**, 103–106 (2010).
- [19] Siviloglou, G. A., Broky, J., Dogariu, A. & Christodoulides, D. N. Ballistic dynamics of Airy beams. *Opt. Lett.* **33**, 207–209 (2008).
- [20] Broky, J., Siviloglou, G. A., Dogariu, A. & Christodoulides, D. N. Self-healing properties of optical Airy beams. *Opt. Express* **16**, 12880–12891 (2008).
- [21] Papazoglou, D. G., Efremidis, N. K., Christodoulides, D. N. & Tzortzakis, S. Observation of abruptly autofocusing waves. *Opt. Lett.* **36**, 1842–1844 (2011).
- [22] Ellenbogen, T., Bloch, N. V., Ganany-Padowicz, A. & Arie, A. Nonlinear generation and manipulation of Airy beams. *Nature Photon.* **3**, 395–398 (2009).
- [23] Dolev, I., Ellenbogen, T. & Arie, A. Switching the acceleration direction of Airy beams by a nonlinear optical process. *Opt. Lett.* **35**, 1581 (2010).
- [24] Yu, N., Genevet, P., Kats, M. A., Aieta, F., Tetienne, J.P., Capasso, F., Gaburro, Z. Light propagation with phase discontinuities: generalized laws of reflection and refraction. *Science* **334**, 333–337 (2011).
- [25] Chen, X.Z., Huang, L.L., Mühlender, H., Li, G.X., Bai, B.F., Tan, Q.F., Jin, G.F., Qiu, C.W.,

- Zhang, S. & Zentgraf, T. Dual-polarity plasmonic metalens for visible light. *Nature Commun.* **3**, 1198 (2012).
- [26] Ni, X., Emani, N. K., Kildishev, A., V., Boltasseva, A. & Shalaev, V. M. Broadband light bending with plasmonic nanoantennas. *Science* **335**, 427 (2012).
- [27] Lin, D., Fan, P., Hasman, E. & Brongersma, M. L. Dielectric gradient metasurface optical elements. *Science* **345**, 298–302 (2014).
- [28] Arbabi, A., Horie, Y., Bagheri, M. & Faraon, A. Dielectric metasurfaces for complete control of phase and polarization with subwavelength spatial resolution and high transmission. *Nature Nanotech.* **10**, 937–943 (2015).
- [29] Tymchenko, M., Gomez-Diaz, J. S., Lee, J., Nookala, N., Belkin, M. A. & Alù, A. Gradient nonlinear Pancharatnam-Berry metasurfaces. *Phys. Rev. Lett.* **115**, 207403 (2015).
- [30] Ren, H., Li, X., Zhang, Q. & Gu, M. On-chip noninterference angular momentum multiplexing of broadband light. *Science* **352**, 805–809 (2016).
- [31] Wang, S. M., Wu, P. C., Su, V. C., Lai, Y. C., Chen, M. K., Kuo, H. Y., Chen, B. H., Chen, Y. H., Huang, T. T., Wang, J. H., Lin, R. M., Kuan, C. H., Li, T., Wang, Z. L., Zhu, S. N., Tsai, D. P. A broadband achromatic metalens in the visible. *Nature Nanotech.* **13**, 227-232 (2018).
- [32] Mueller, J. P. B., Rubin, N. A., Devlin R. C., Groever B. & Capasso, F. Metasurface Polarization Optics: Independent Phase Control of Arbitrary Orthogonal States of Polarization *Phys. Rev. Lett.* **118**, 113901 (2017).
- [33] Devlin, R. C., Ambrosio, A., Rubin, N. A., Mueller, J. B. & Capasso, F. Arbitrary spin-to-orbital angular momentum conversion of light. *Science*, **358**, 896-901 (2017).
- [34] Lalanne, P., Astilean, S., Chavel, P., Cambriil, E. & Launois, H. Blazed binary subwavelength gratings with efficiencies larger than those of conventional échelette gratings. *Opt. Lett.* **23**, 1081–1083 (1998).
- [35] Khorasaninejad, M., Chen, W. T., Devlin, R. C., Oh, J., Zhu, A. Y., Capasso, F. Metalenses at visible wavelengths: diffraction-limited focusing and subwavelength resolution imaging. *Science* **352**, 1190–1194 (2016).

[36] Devlin, R.C., Khorasaninejad, M., Chen, W.T., Oh, J., Capasso, F. Broadband high-efficiency dielectric metasurfaces for the visible spectrum. *PNAS* **113**,10473–10478 (2016).

[37] Sun, J. & Wu, S.-T., Recent advances in polyer network liquid crystal spatial light modulators. *J. Polym. Sci. B* **52**, [183–192 \(2014\)](#).

[38] Kaganovsky, Y. & Heyman, E. Wave analysis of Airy beams. *Opt. Express* **18**, 8440–8452 (2010).

[39] Froehly, L., Courvoisier, F., Mathis, A., Jacquot, M., Furfaro, L., Giust, R., Lacourt, P. A. & Dudley, J. M. Arbitrary accelerating micron-scale caustic beams in two and three dimensions. *Opt. Express* **19**, 16455–16465 (2011).

Acknowledgements

The work is supported in part by the Key Research and Development Program from Ministry of Science and Technology of China under Grant No. 2016YFA0202100 and 2017YFA0303700 and National Natural Science Foundation of China under Grant No. 61575092 and 11774163. C. Z., W. Z., and A. A. acknowledge support under the Cooperative Research Agreement between the University of Maryland and the National Institute of Standards and Technology Center for Nanoscale Science and Technology, Award #70NANB14H209, through the University of Maryland.

Competing Interests

The authors declare no competing financial interests.

Figures and Captions

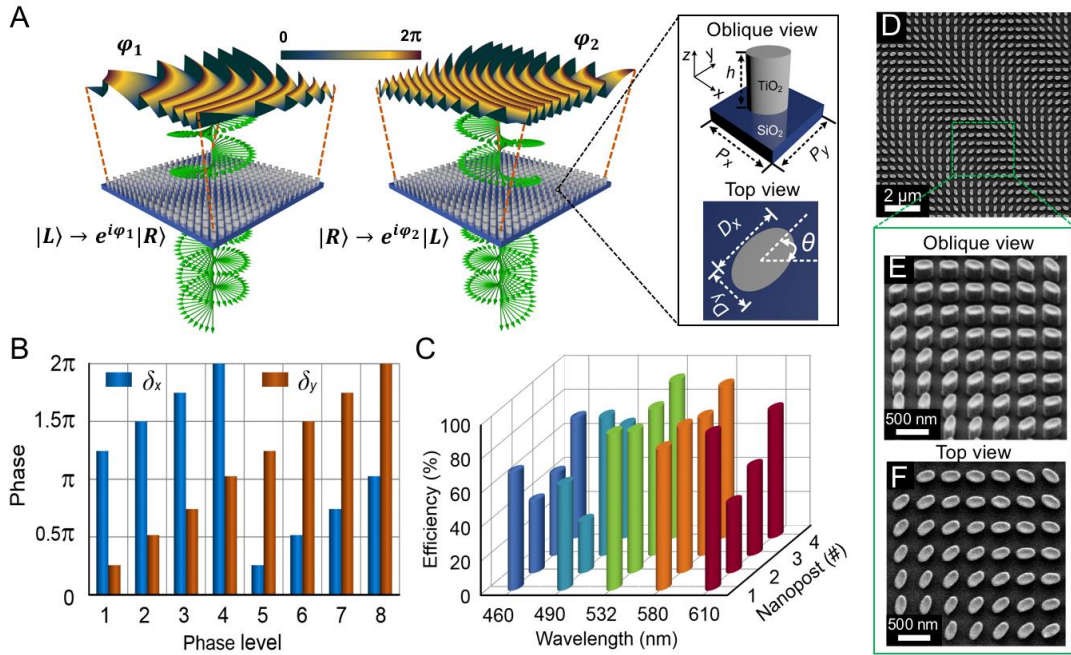


Fig. 1. Photonic spin-controlled ALB metasurface generator. (A) Schematic diagram of the metasurface device capable of providing two independent phase profiles, φ_1 and φ_2 , respectively for normally incident LCP and RCP light. Inset: perspective and top view of the metasurface unit cell formed by elliptical amorphous TiO_2 nanopost sitting on a silica substrate. (B) Calculated phase shifts, δ_x and δ_y , for different phase levels at a free-space wavelength of 532 nm. Each level corresponds to a specific TiO_2 nanopost birefringent wave-plate. (C) Calculated polarization conversion efficiency of the chosen nanopost structures at five different wavelengths (460 nm, 490 nm, 532 nm, 580 nm and 610 nm) across the visible range. (D)-(F) SEM images of the fabricated metasurface device. The SEM image respectively show (D) a top view of large area, (E) zoomed view at an oblique angle and (F) corresponding top view for the same area.

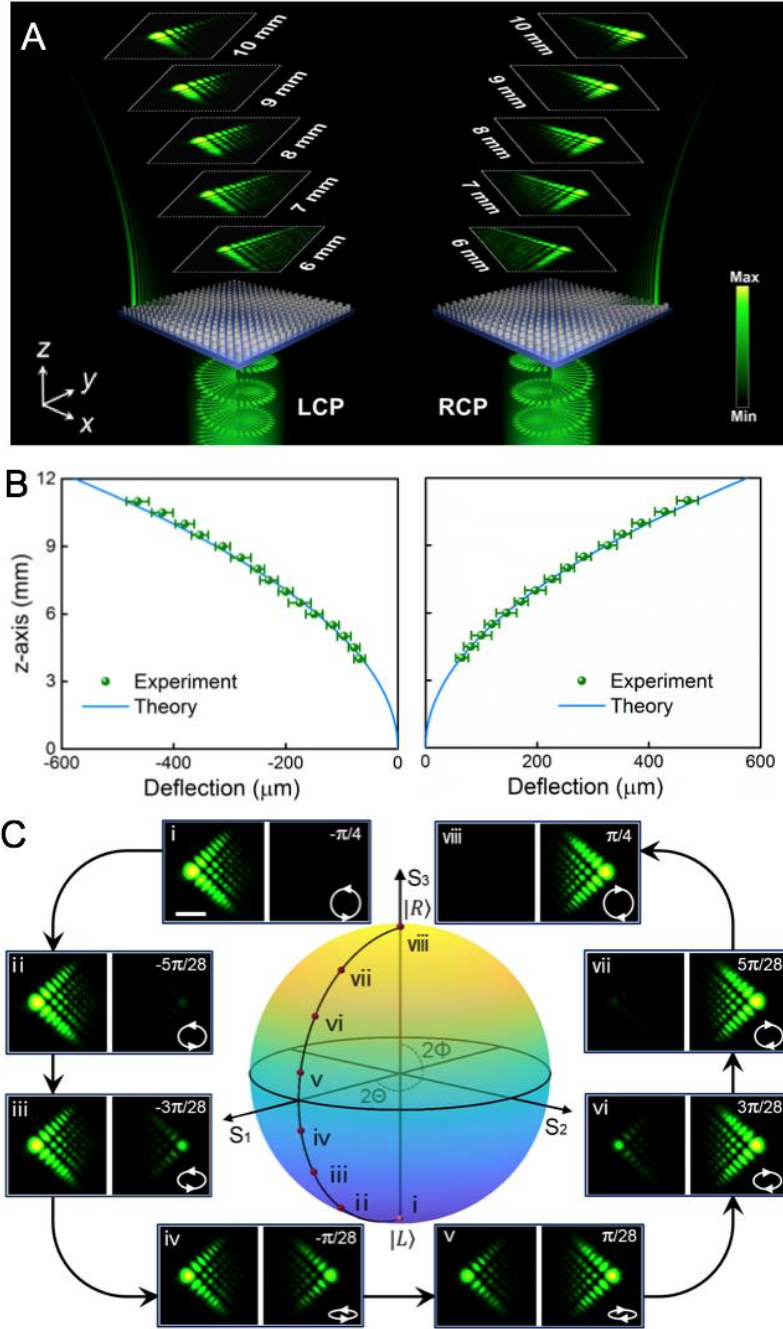


Fig. 2. Generation of switchable optical Airy beams with opposite acceleration directions. (A) Schematic diagram of the experimental generation of optical Airy beams by the metasurface. The images in the white dashed frame show measured output intensities in the x - y plane along propagation trajectories for the incident light in LCP (left) and RCP (right). The wavelength of the incident light is 532 nm. (B) Experimentally measured (sphere) and theoretically calculated (solid line) Airy beams' propagation trajectories. The uncertainties are one standard deviation of deflection distance for repeated experimental measurements (four in total). (C) Evolution of the

output beams versus incident spin states. All the intensity profiles are taken at $z = 8$ mm. The circles with arrows on the Poincaré sphere show eight experimental incident spin states corresponding to intensity profiles i-viii. Scale bar for all the optical intensity images in (C), $50 \mu\text{m}$.

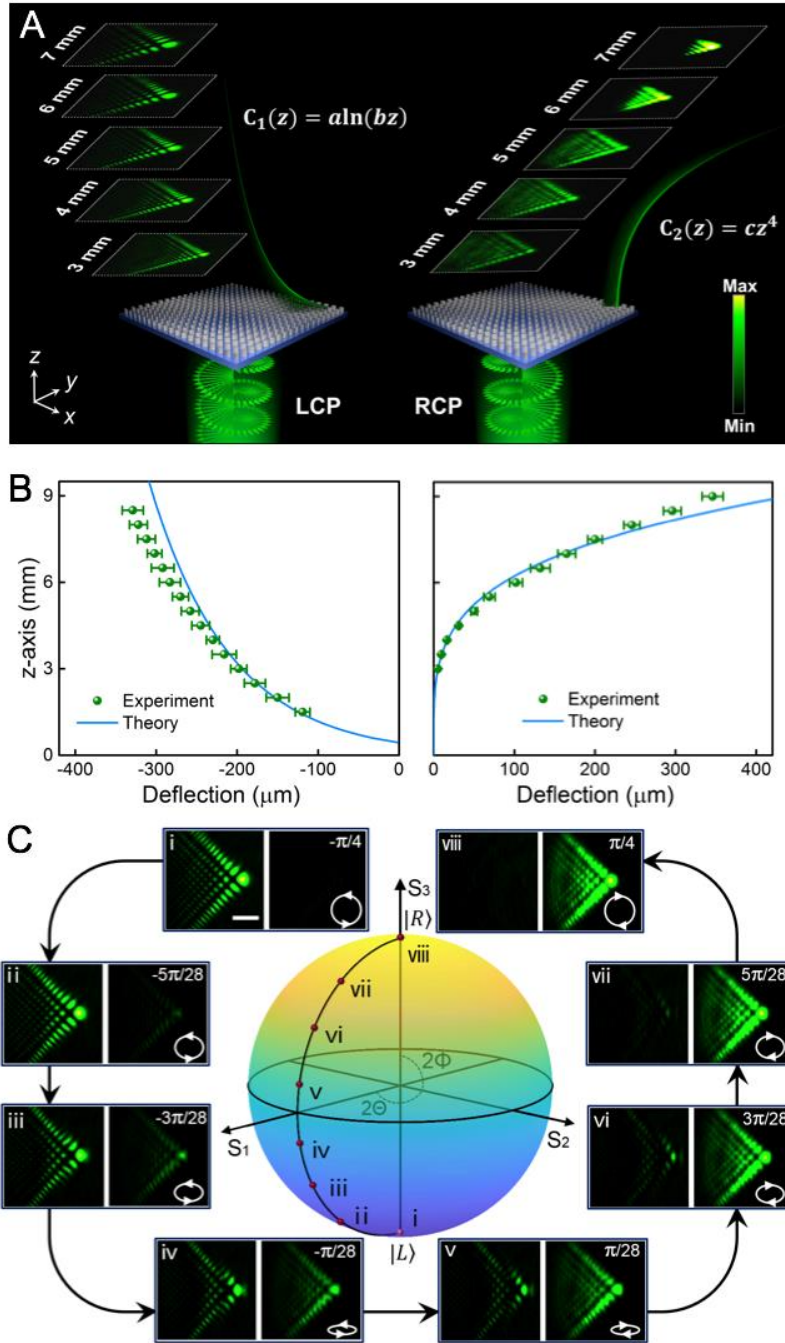


Fig. 3. Generation of switchable ALBs with different caustic trajectories. (A) Schematic diagram of the experimental generation of ALBs respectively following natural logarithm and biquadratic caustic trajectories by metasurface. The images in the white dashed frame show measured output intensities in the x - y plane along propagation trajectories for the incident light

with LCP (left) and RCP (right). (B) Experimentally measured (sphere) and theoretically calculated (solid line) two ALBs' propagation trajectories for LCP and RCP light. The uncertainties are one standard deviation of deflection distance for repeated experimental measurements (four in total). (C) Evolution of the output beams versus incident spin states. All the intensity profiles are taken at $z = 5$ mm. The circles with arrows on the Poincaré sphere show 8 experimental incident spin states corresponding to intensity profiles i-viii. Scale bar for all the intensity images in (C), $50 \mu\text{m}$.

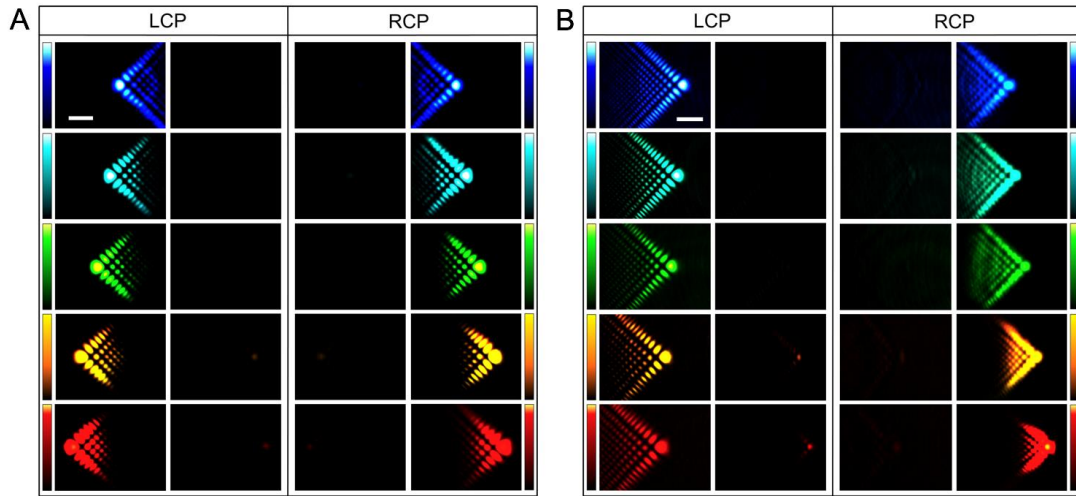


Fig. 4. Multi-wavelength generation and control of ALBs. Experimentally measured intensity profiles of the generated (A) optical Airy beams ($z = 8$ mm) and (B) generalized acceleration light beams ($z = 5$ mm) by the two designed metasurface devices at free-space wavelengths of $\lambda_0 = 460$ nm, 490 nm, 532 nm, 580 nm, 610 nm. Scale bar for all the intensity images is $50 \mu\text{m}$.

Supplementary Materials for

Generation of photonic spin-controlled accelerating light beams along arbitrary curved trajectories

SI: Derivation of the Jones matrix J and its eigenvalues and eigenvectors.

Assuming input polarization states $\{|\alpha^+\rangle, |\alpha^-\rangle\}$ upon which the metasurface should impart two independent phase profiles, $\varphi_1(x, y)$ and $\varphi_2(x, y)$, be given by orthogonal polarization states $|\alpha^+\rangle = \begin{bmatrix} \alpha_1^+ \\ \alpha_2^+ \end{bmatrix}$ and $|\alpha^-\rangle = \begin{bmatrix} \alpha_1^- \\ \alpha_2^- \end{bmatrix}$. We can find a design of a linearly birefringent metasurface where the output polarization states become $\{ |(\alpha^+)^*\rangle, |(\alpha^-)^*\rangle \}$; denoting complex conjugate of input polarization states. This means that they have the same states as the input states with flipped handedness. Such device can be described by Jones matrix $J(x, y)$ that simultaneously satisfies

$$J(x, y) |\alpha^+\rangle = e^{i\varphi_1(x, y)} |(\alpha^+)^*\rangle \quad (S1)$$

and

$$J(x, y) |\alpha^-\rangle = e^{i\varphi_2(x, y)} |(\alpha^-)^*\rangle \quad (S2)$$

In our design, the input polarization states are orthogonal circular polarizations states:

$$|L\rangle = \begin{bmatrix} 1 \\ i \end{bmatrix} \quad (S3)$$

$$|R\rangle = \begin{bmatrix} 1 \\ -i \end{bmatrix} \quad (S4)$$

Then, the original system can be expressed as

$$J(x, y) \begin{bmatrix} 1 \\ i \end{bmatrix} = e^{i\varphi_1(x, y)} \begin{bmatrix} 1 \\ -i \end{bmatrix} \quad (S5)$$

and

$$J(x, y) \begin{bmatrix} 1 \\ -i \end{bmatrix} = e^{i\varphi_2(x, y)} \begin{bmatrix} 1 \\ i \end{bmatrix} \quad (S6)$$

Upon matrix inversion of Eq. S5 and S6 we obtain,

$$J(x, y) = \begin{bmatrix} e^{i\varphi_1(x, y)} & e^{i\varphi_2(x, y)} \\ -ie^{i\varphi_1(x, y)} & ie^{i\varphi_2(x, y)} \end{bmatrix} \begin{bmatrix} 1 & 1 \\ i & -i \end{bmatrix}^{-1} \quad (S7)$$

Then, we can show that the desired matrix $J(x, y)$ is

$$J(x, y) = \frac{1}{2} \begin{bmatrix} e^{i\varphi_1(x, y)} + e^{i\varphi_2(x, y)} & ie^{i\varphi_2(x, y)} - ie^{i\varphi_1(x, y)} \\ ie^{i\varphi_2(x, y)} - ie^{i\varphi_1(x, y)} & -e^{i\varphi_1(x, y)} - e^{i\varphi_2(x, y)} \end{bmatrix} \quad (\text{S8})$$

where $\varphi_1(x, y)$ and $\varphi_2(x, y)$ are phase profiles of arbitrary accelerating beams. This matrix provides a general form for conversion between two arbitrary accelerating beams and even arbitrary structured light. By calculating Jones matrix $J(x, y)$, we can obtain the eigenvalues as

$$\xi_1 = e^{i[\frac{1}{2}(\varphi_1(x, y) + \varphi_2(x, y))]} \quad \xi_2 = e^{i[\frac{1}{2}(\varphi_1(x, y) + \varphi_2(x, y)) - \pi]} \quad (\text{S9})$$

and eigenvectors as

$$|r_1\rangle = \begin{bmatrix} \cos\frac{1}{4}[\varphi_1(x, y) - \varphi_2(x, y)] \\ \sin\frac{1}{4}[\varphi_1(x, y) - \varphi_2(x, y)] \end{bmatrix} \quad |r_2\rangle = \begin{bmatrix} -\sin\frac{1}{4}[\varphi_1(x, y) - \varphi_2(x, y)] \\ \cos\frac{1}{4}[\varphi_1(x, y) - \varphi_2(x, y)] \end{bmatrix} \quad (\text{S10})$$

Thus, the Jones matrix $J(x, y)$ can be decomposed into canonical form $J = P\Lambda P^{-1}$, where Λ is a diagonal matrix and P is an invertible matrix. We can write the Jones matrix for the control and conversion between two arbitrary optical beams as

$$J(x, y) = P\Lambda P^{-1} = \begin{bmatrix} \cos\frac{1}{4}[\varphi_1(x, y) - \varphi_2(x, y)] & -\sin\frac{1}{4}[\varphi_1(x, y) - \varphi_2(x, y)] \\ \sin\frac{1}{4}[\varphi_1(x, y) - \varphi_2(x, y)] & \cos\frac{1}{4}[\varphi_1(x, y) - \varphi_2(x, y)] \end{bmatrix} \cdots \\ \begin{bmatrix} e^{i[\frac{1}{2}(\varphi_1(x, y) + \varphi_2(x, y))]} & 0 \\ 0 & e^{i[\frac{1}{2}(\varphi_1(x, y) + \varphi_2(x, y)) - \pi]} \end{bmatrix} \begin{bmatrix} \cos\frac{1}{4}[\varphi_1(x, y) - \varphi_2(x, y)] & -\sin\frac{1}{4}[\varphi_1(x, y) - \varphi_2(x, y)] \\ \sin\frac{1}{4}[\varphi_1(x, y) - \varphi_2(x, y)] & \cos\frac{1}{4}[\varphi_1(x, y) - \varphi_2(x, y)] \end{bmatrix} \quad (\text{S11})$$

Since Jones matrix $J(x, y)$ works in the linear polarization basis and P can be regarded as a rotation matrix for the matrix Λ , we can obtain that the phase shifts are $\delta_x(x, y) = [\varphi_1(x, y) + \varphi_2(x, y)]/2$ and $\delta_y(x, y) = [\varphi_1(x, y) + \varphi_2(x, y)]/2 - \pi$ and the rotation angle is $\theta(x, y) = [\varphi_1(x, y) - \varphi_2(x, y)]/4$.

SII: Sample fabrication

500 μm -thick, double-side polished fused silica substrates were first prime-vapor-coated with a monolayer of hexamethyldisilazane (HMDS) and then spin-coated with a layer of 600 nm thick, positive-tone electron beam (e-beam) resist. Afterwards, the samples were coated with a layer of 10 nm thick Aluminum (Al) via thermal evaporation, which suppressed the charging effect during the subsequent e-beam lithography step. The e-beam lithography was performed at an accelerating voltage of 100 kV and beam current of 2 nA. The samples were developed in hexyl-acetate for 120 s. Next, the patterned samples were coated with TiO_2 using atomic layer deposition (ALD). The ALD was done at a low temperature of 363 K to avoid deformation of the resist pattern. After the ALD, the over-coated TiO_2 layer was etched by the inductively-coupled-plasma reactive ion etching (ICP-RIE), with a gas mixture of Cl_2 and BCl_3 . The etching was stopped when the over-coated TiO_2 had been fully removed and the e-beam resist was exposed. Finally, the samples were exposed to UV irradiation, followed by soaking in n-methyl-2-pyrrolidone, which removed the resist and produced the array of TiO_2 nanoposts with pre-designed geometries.

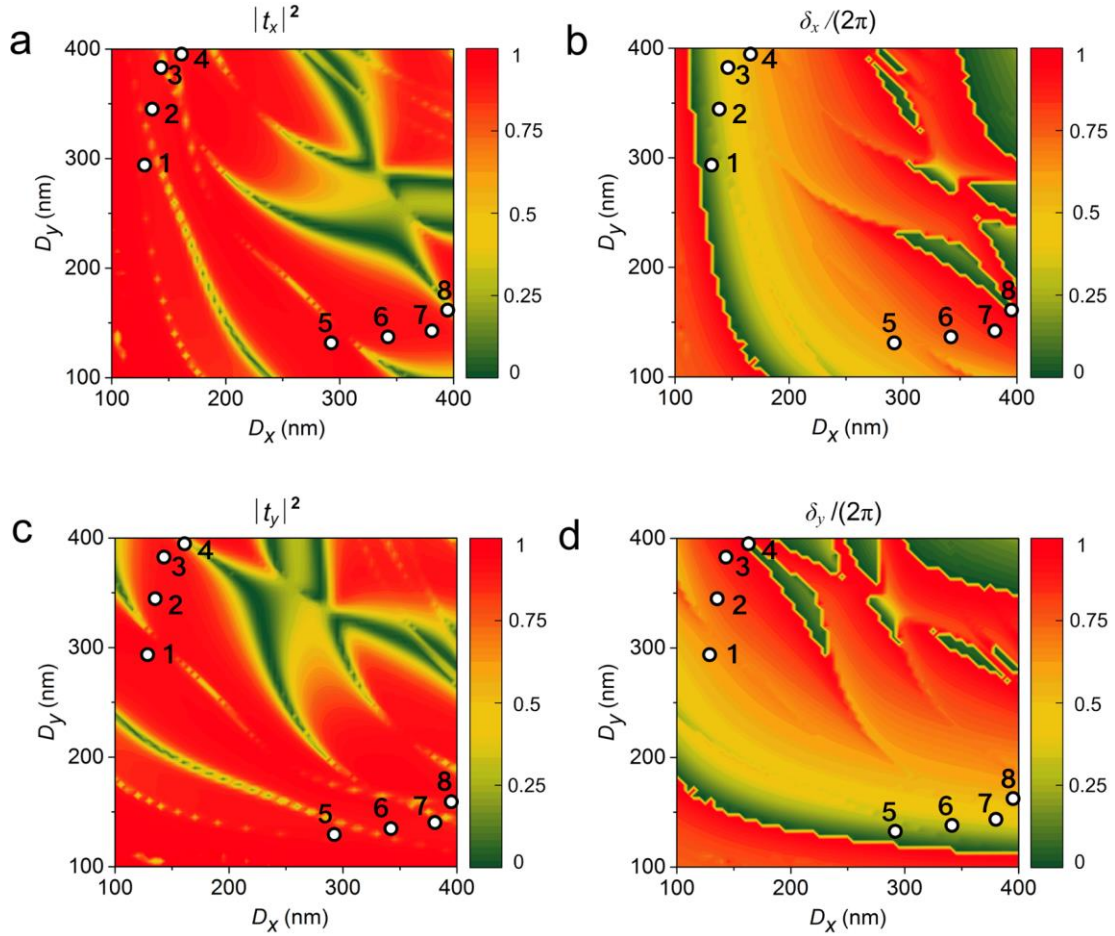


Figure S1. Calculated cross-polarized transmission coefficients (a. $|t_x|^2$; c. $|t_y|^2$) and phase shifts (b. δ_x ; d. δ_y) as a function of elliptical nanopost diameters (D_x , D_y) at the wavelength of 532 nm. The chosen structural parameters (white dots) for four fundamental nanopost structures is nanopost #1: $D_x=130$ nm, $D_y=295$ nm; nanopost #2: $D_x=135$ nm, $D_y=345$ nm; nanopost #3: $D_x=140$ nm, $D_y=385$ nm; nanopost #4: $D_x=160$ nm, $D_y=395$ nm. The other four mirror structures #5 ~ #8 can be obtained just by switching D_x and D_y on nanopost #1-4.

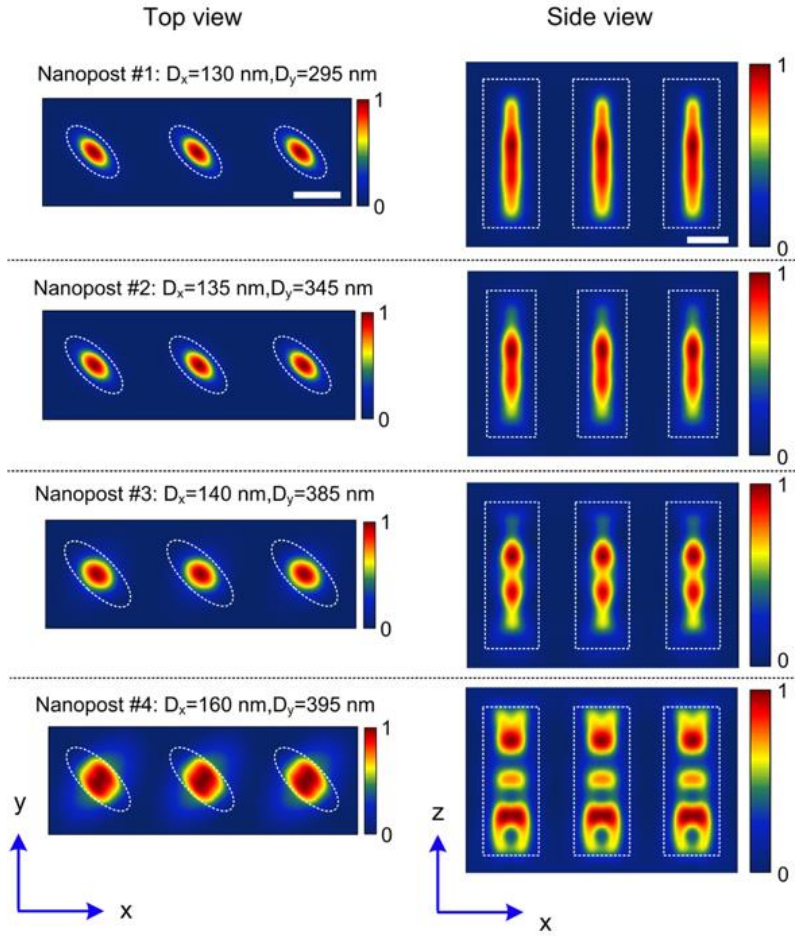


Figure S2. Top views (left: xy cross-section) and side views (right: xz cross-section) of the normalized magnetic field intensity in a periodic array for different nanopost structures. The array of nanoposts are rotated by 45° with respect to the square lattice. A plane wave with y -polarization is normally incident on the TiO_2 nanoposts from the substrate side. The boundaries of the nanoposts are depicted by dashed white lines. Scale bars represent 200 nm in all directions.

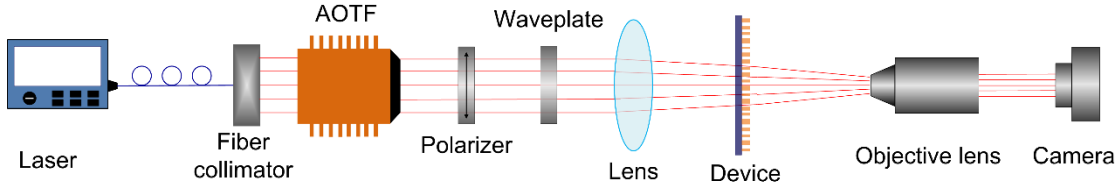


Figure S3. Schematic illustration of the measurement setup used for characterization of metasurface devices generating switchable accelerating light beams. The quarter-wave plate (QWP) is rotated to convert the polarization of incident light from LCP to RCP. AOTF: Acousto-Optic Tunable Filter system.

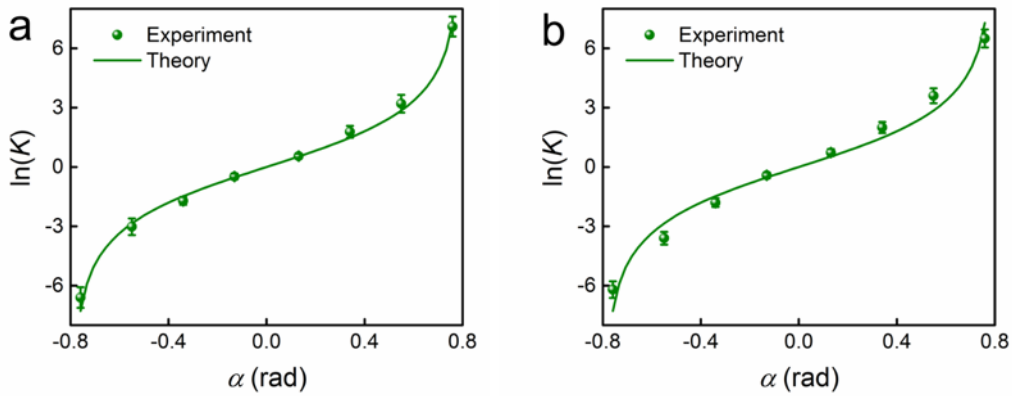


Figure S4. Calculated and measured intensity ratio K (in logarithmic scale) between $|R\rangle|A_r\rangle$ and $|L\rangle|A_l\rangle$ as a function of the QWP rotation angle α for the metasurface devices generating (a) two Airy beams and (b) biquadratic and natural logarithm beams. The uncertainties are one standard deviation of deflection distance for repeated experimental measurements (four in total).

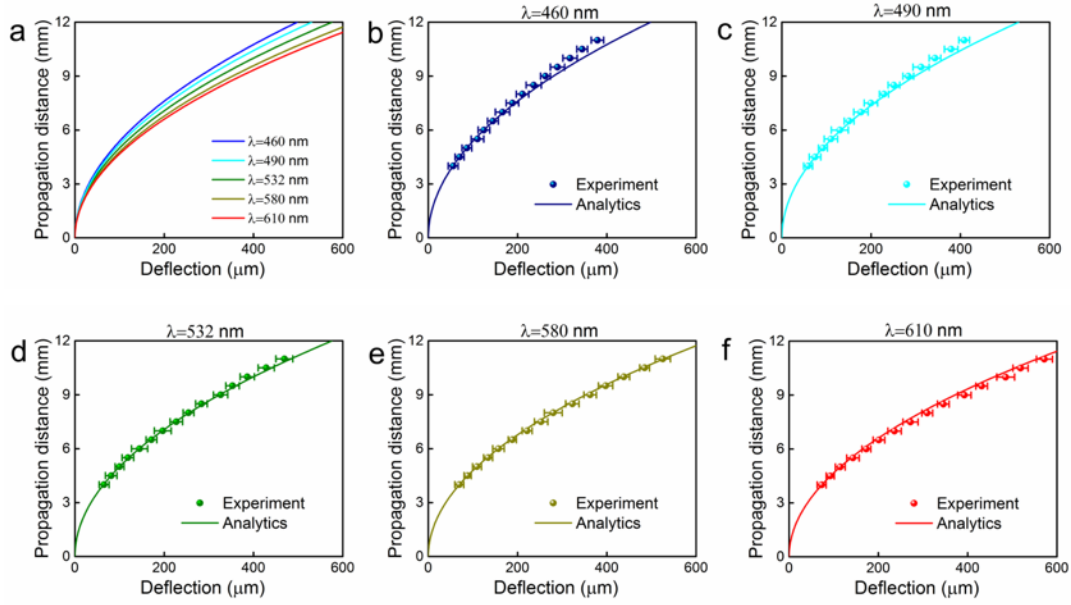


Figure S5. (a) Calculated propagation trajectories of the metasurface-generated Airy beams under the illumination at different wavelengths. (b)-(f) Experimentally measured propagation trajectories of Airy beams at different wavelengths. The uncertainties are one standard deviation of deflection distance for repeated experimental measurements (four in total).

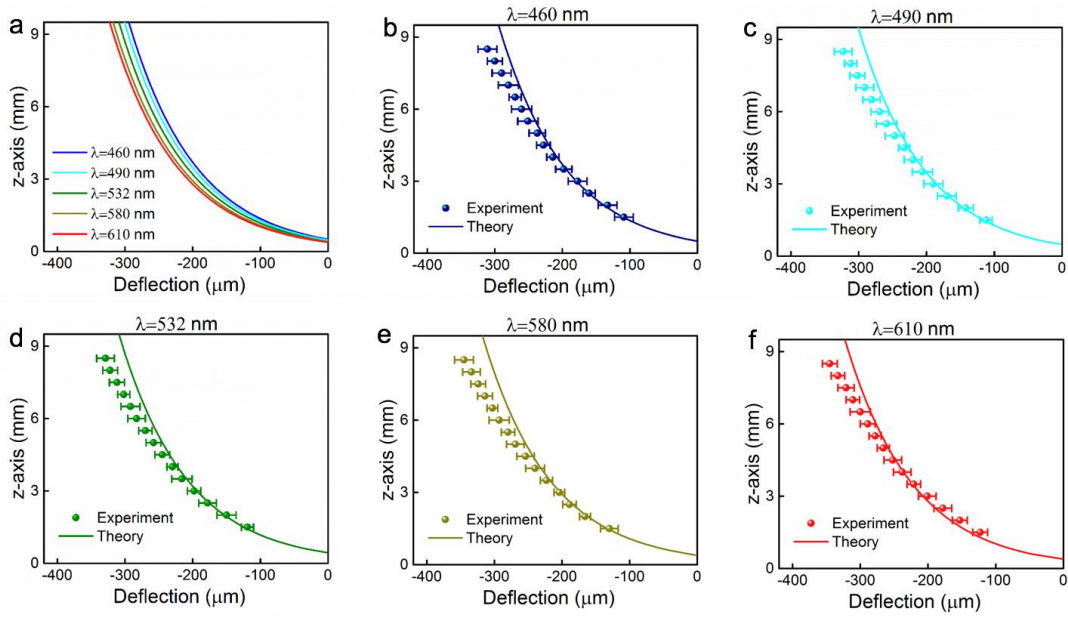


Figure S6. (a) Calculated propagation trajectories of the metasurface-generated accelerating beam following natural logarithm caustic trajectories under the illumination at different wavelengths. (b)-(f) Experimentally measured propagation trajectories of accelerating beams at different wavelengths. The uncertainties are one standard deviation of deflection distance for repeated experimental measurements (four in total).

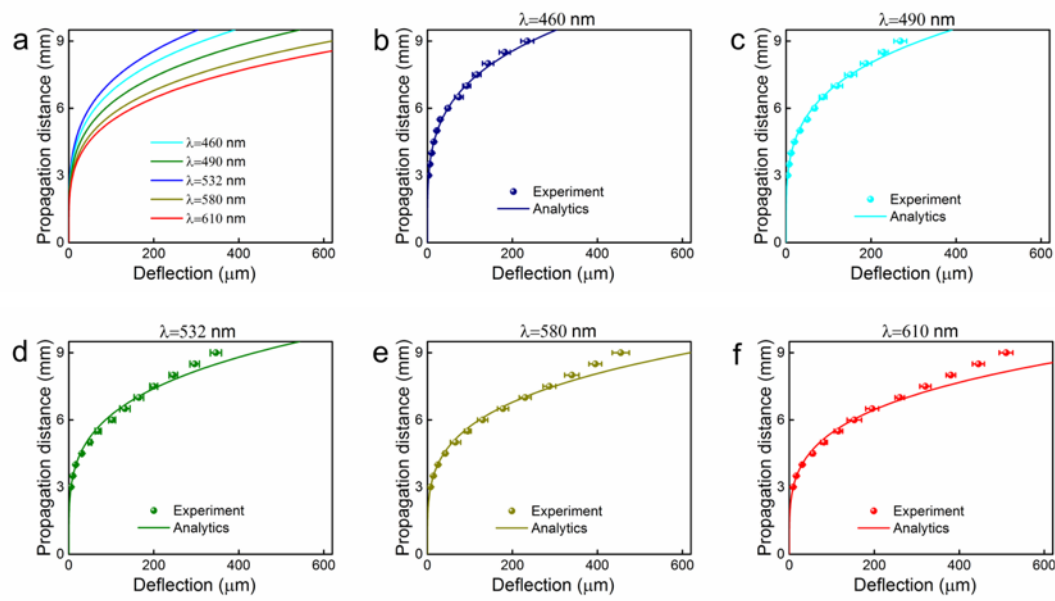


Figure S7. (a) Calculated propagation trajectories of the metasurface-generated accelerating beam following biquadratic caustic trajectories under the illumination at different wavelengths. (b)-(f) Experimentally measured propagation trajectories of accelerating beams at different wavelengths. The uncertainties are one standard deviation of deflection distance for repeated experimental measurements (four in total).

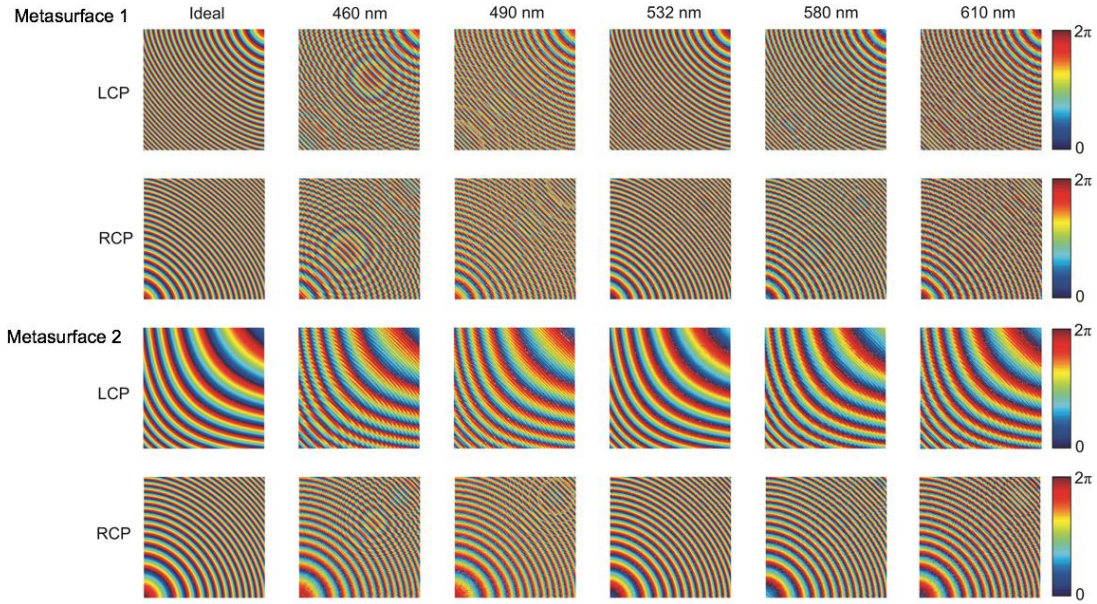


Figure S8. The calculated phase profiles of two metasurfaces for LCP and RCP light at multiple wavelengths. The horizontal and vertical axes of each subplot represent a spatial area of $450 \mu\text{m} \times 450 \mu\text{m}$ of the fabricated metasurface samples 1 & 2. The color scales represent the phase profiles of the metasurfaces measured in Figure 3 & 4, which are designed to achieve the generation and switching between two arbitrary accelerating light beams to follow different caustic trajectories in free-space. As shown in this figure, the phase profiles of this TiO_2 metasurface are very similar for the selected multi-wavelengths.